

Damage tolerance of a micro-architected adhesive joint

Kevin Maloney and Norman Fleck*

Cambridge University Engineering Department, Trumpington Street,
Cambridge, CB2 1PZ, UK

Abstract

Butt joints have been manufactured from aluminium alloy substrates of interlocking square-wave architecture and silyl-modified polymer (SMP) adhesive. The macroscopic traction versus opening separation responses of the butt joints have been measured for selected values of square-wave amplitude and thickness of adhesive layer. The mechanisms of adhesive failure at selected locations in the square-wave joint are determined by micro X-ray computed tomography and optical fractography. Additional insight into the failure mechanisms of the square-wave joint is obtained by performing tensile tests on planar butt joints and by performing double-lap shear tests on planar joints. The failure mechanisms in the square-wave joint are a combination of those observed in the butt and double-lap shear joints, and consequently a simple model for the strength and toughness of the square-wave joint is developed. A design map is constructed for the strength, toughness and damage-tolerance of the square-wave micro-architecture in order to generate the optimal topology for a given application.

Keywords: Patterned interfaces; Elastomers; Adhesive joint; Cavitation; Toughening

*Corresponding author: naf1@eng.cam.ac.uk

1. Introduction

Elastomeric joints find widespread application throughout many industries but are prone to failure by cavitation within the joint. A large aspect ratio within the joint promotes high hydrostatic tension in the nearly-incompressible elastomer and thereby gives rise to cavitation. One strategy to increase joint strength (and toughness) is to alter the shape of the joint to that of interlocking fingers so that any load is carried by shear instead of tension. The purpose of the present study is to explore the potential of this approach.

The behaviour of interlocking interfaces subject to a remote tensile load has been explored in recent years (Li et al., 2011). For example, the remote tensile strength of a joint between two composite materials can be increased by fifty percent by introducing triangular fingers along the bondline (Boyd et al., 2006). Fractal hierarchy can greatly reduce the risk of catastrophic failure by promoting widespread mechanical interlocking, resulting in a safer overall structure (Li et al., 2012).

A number of experimental and numerical studies investigating adhesive joints with periodic, interlocking interfacial features have shown that interlocking interfaces can provide greater stiffness, strength and toughness than planar interfaces due to increased real surface area and the generation of local shear stresses rather than tensile peel stresses, which often cause catastrophic interfacial failure (Cordisco et al., 2016; Haghpanah et al., 2014; Li et al., 2011; Suzuki et al., 2013; Zavattieri et al., 2007). The periodic interface is characterised by an amplitude A , wavelength λ and joint thickness t . In general, the strength and toughness of the interface will depend upon (A, λ, t) , thereby giving the opportunity for the optimisation of joint geometry for any given application.

Reedy and colleagues (2007) developed a finite element cohesive zone model to determine the toughness of an interface with a nanoscale square-wave pattern. In their words, “the most important finding is that the apparent interfacial toughness scales directly with real interfacial area,” and the apparent toughness of a square-wave interface can be increased by increasing the real interfacial area, i.e. by increasing the amplitude of the square wave. They observe that the crack growth process along a square-wave interface is discontinuous, with crack initiation occurring ahead of the tip of the stalled continuous crack, and note that the toughness of a square-wave interface is greater than that of a sinusoidal interface. Simultaneously, Zavattieri et al (2007) investigated the fracture toughness of sinusoidal interfaces using a finite element cohesive zone model. They also found that the macroscopic

toughness scales linearly with the amplitude of the sinusoidal interface. Recent experimental results from Cordisco, Zavattieri, Hector, & Carlson (2016) for the Mode I behaviour of DCB joints with sinusoidal interfaces also support the notion that toughness scales with the amplitude of waviness of an adhesive joint.

1.1 Scope of Study

The tensile traction versus separation (T - δ) response of a periodic “square-wave” adhesive joint is measured as a function of adhesive layer thickness t and square-wave amplitude A . The joints are made from silyl-modified polymer (SMP) adhesive sandwiched between 6082 T651 aluminium alloy substrates. Benchmarking tests are performed on planar adhesive joints in both a tensile peel mode (butt joints) and a shear mode (lap joints). The strength, toughness (as defined by the area under the T - δ curve) and critical separation are compared for flat interfaces and square-wave interfaces. A simple mechanics analysis is developed for the T - δ response of the square-wave geometry. Maps are thereby constructed to illustrate the optimal topology as a function of joint architecture from the perspective of strength, toughness or damage tolerance.

2. Materials and Methods

The adhesive joints comprised a two-part, moisture-curing silyl-modified polymer (SMP) adhesive¹ sandwiched between substrates made from aluminium alloy 6082 T651. This adhesive contains filler particles on a scale of 10 μm diameter in order to control the viscosity in the un-cured state. The alloy 6082-T651 was selected because its yield strength (310 MPa) is sufficiently high that it behaves in an elastic manner.

2.1 Specimen Geometry

The square-wave joint is characterised by five parameters: amplitude A , wavelength λ , two adhesive layer thickness parameters t and s and a depth (into page) B , as defined in Figure 1. The depth B , wavelength λ and thickness s were held fixed at 12.8 mm, 28 mm and 1.1 mm, respectively, while the amplitude A was varied in the range 2.5 to 20 mm, and the thickness t

¹ Sabatack Fast, produced by SABA Dinxperlo BV, Industriestraat 3, 7091 DC Dinxperlo, Netherlands.

was varied from 1.1 to 4.0 mm. Numerical values for the geometric parameters are listed in Table 1. Suitably-shaped substrates were water-jet cut from 6082 T651 aluminium alloy plate.

A series of additional tests were performed in order to characterise the SMP adhesive, and to benchmark the tensile response of the square-wave joint against that of a butt joint and a double-lap shear joint. The uniaxial response of the SMP adhesive was measured by casting a dogbone specimen from the adhesive, with geometry defined in Figure 2(a). The specimen geometry of the butt joint, double-lap shear joint and square-wave joint are given in Figure 2(b), (c) and (d), respectively. Numerical values for the various geometric parameters are summarised in Table 2.

2.2 Specimen Preparation

Surface preparation is critical to the formation of a strong adhesive bond. Roughening of the substrates was accomplished by manual polishing using 60 grit emery paper. The surfaces were then cleaned and degreased by wiping with acetone. The adhesive was applied in accordance with the manufacturer's recommendations. A manual applicator gun was used with a static-mixing nozzle. The thickness of the adhesive layer was adjusted by shims prior to infiltration of the gap by the adhesive. All specimens were cured in ambient air for one week at room temperature. Dogbone specimens were fabricated using custom, non-stick PTFE moulds. After each mould was filled with adhesive, the top surface of each specimen was smoothed with a flat-edged PTFE strip.

2.3 Test Procedure

The majority of mechanical tests were conducted using a screw-driven test machine². The tensile load on each specimen was measured by the load cell of the test machine, while the displacement was measured by the test machine and by a laser extensometer³. Uniaxial tension tests on dogbone specimens of SMP adhesive were performed in accordance with ASTM D638-14 (Anon 2014) at machine displacement rates in the range $0.01 \text{ mm}\cdot\text{s}^{-1}$ to $1000 \text{ mm}\cdot\text{s}^{-1}$ to characterise the viscoelastic nature of the adhesive.

² There was no need to measure the stress versus strain response for the aluminium alloy substrates as they behaved in an elastic manner throughout all tests.

³ Electronic Instrument Research Laser Extensometer, Model LE-05.

The tests on butt joints, double-lap shear joints and square-wave joints were performed using a machine displacement rate in the range $7 \times 10^{-3} \text{ mm}\cdot\text{s}^{-1}$ to $3 \times 10^{-2} \text{ mm}\cdot\text{s}^{-1}$ corresponding to a normalised displacement rate $\dot{\delta}/t$ of approximately $7 \times 10^{-3} \text{ s}^{-1}$. At least three specimens of each joint geometry were tested, and uncertainty values are calculated as the standard deviation of each set of specimens.

During each adhesive joint test, images of the adhesive layer were recorded in order to monitor the failure progression within the joint. An optical camera⁴ was used with a frame rate of 0.5 frames per second.

3. Results and Discussion for Bulk Adhesive and Planar Joints

3.1 Bulk Properties of Elastomeric Adhesive

The uniaxial tensile stress versus strain response of the SMP adhesive is summarised in Figure 3(a) for three values of nominal strain rate ($3 \times 10^{-3} \text{ s}^{-1}$, $3 \times 10^{-1} \text{ s}^{-1}$ and 30 s^{-1}). Both nominal and true stress versus strain responses are presented. The shape of the stress versus strain response is independent of strain rate but the strain to failure (and associated tensile strength) is mildly sensitive to strain rate. As the strain rate is increased from $3 \times 10^{-3} \text{ s}^{-1}$ to 30 s^{-1} , the nominal failure strength σ_c increases from 2.5 MPa to 3.6 MPa and the true (logarithmic) strain to failure increases from 0.95 to 1.42, while the Young's modulus E is almost constant at $2.5 \pm 0.2 \text{ MPa}$. The SMP adhesive shows the characteristic Mullins effect (hysteresis) upon unloading and reloading, as illustrated by the typical nominal stress-strain response in Figure 3(b) for $\dot{\epsilon} = 3 \times 10^{-3} \text{ s}^{-1}$.

3.2 Properties of Planar Adhesive Joints

3.2.1 Tensile Butt Joints

The tensile response of butt joints with planar interfaces is described in terms of the shape factor S defined, in the usual manner, as follows. Consider an elastomeric adhesive joint of thickness t , width w and depth B . Introduce the shape factor S as the loaded cross-sectional area wB divided by the area of the free surfaces $2t(w+B)$ (Gent and P. B. Lindley 1959; Hattori and Takei 1950), such that

⁴ PixeLINK PL-B776U Aptina MT9T001 Machine Vision Camera.

$$S = \frac{wB}{2t(w + B)} \quad (1)$$

Four normal traction T_n versus normalised separation δ_n/t curves are presented in Figure 4(a) and these are compared against the nominal stress versus nominal strain response of a dogbone specimen. The constraint level of the adhesive joint is dictated by the adhesive layer thickness t (over the range 1.1 mm to 4.0 mm), the specimen width w (ranging from 13 mm to 50 mm) and the specimen depth B (12.8 mm). The nominal traction versus separation response of each adhesive butt joint is non-linear, with a pronounced knee. In contrast, the dogbone displays an almost linear behaviour. As the shape factor increases, the knee becomes more pronounced. The non-linearity is due to the development of ‘damage’ within the adhesive layer in the form of cavitation.

The tensile response of a representative butt joint of adhesive layer thickness $t = 1.1$ mm, $w = 13$ mm, $B = 12.8$ mm and $S = 2.9$ is shown in Figure 4(b). At selected points (i) to (iv) of deformation, the test was stopped and the morphology of damage within the adhesive layer was examined using computed tomography (CT) imaging. Images of three planes P_1 , P_2 , and P_3 normal to the loading direction are shown at each point (i) to (iv) in Figure 4(c). The two planes nearest the substrates (P_1 and P_3) are each located 0.2 mm from the adjacent interface, and the plane P_2 is at the mid-plane of the adhesive layer. In the unstressed state (i), a small void is detected near each interface, while no damage is observed on the P_2 -plane. As indicated in the T_n - δ_n response, cavitation develops when the traction is increased to 1.6 MPa, and many small spherical voids are now observed on all three planes at a traction of 1.8 MPa, as denoted (ii) in Figure 4(b) and (c). A greater density of small voids is evident near each interface than along the mid-plane, which displays a collection of larger, more-dispersed voids. Each of the two voids observed in the unstressed state experiences considerable growth, each from an initial diameter of approximately 0.5 mm to an approximate diameter of 1.5 mm at (ii). With increasing separation, the traction increases and void growth is non-uniform such that the two dominant voids continue to grow with almost no expansion of neighbouring smaller voids through point (iii) towards point (iv), at which time each of the two large voids is no longer spherical, and each appears bound by the aluminium substrates, as they are both visible on each of the three planes in (iv). Ultimate failure occurs by worm-like coalescence of voids, as shown in the CT image of the failure surface at point (v).

For all four points (i) through (iv), negligible voiding is observed within one millimetre of the periphery of the specimen (i.e. approximately one adhesive layer thickness). This is due to the fact that the stress triaxiality is reduced near the free surface of the adhesive layer.

Four critical parameters of tensile butt joints are presented as functions of shape factor S in Figure 5. They are (i) the peak normal traction T_{nc} , (ii) the normalised separation at peak traction δ_{nc}/t , (iii) the dissipated energy normalised by the adhesive layer thickness Γ_n/t , and (iv) the normalised elastic modulus E^*/E . As the shape factor increases, the peak traction rises to a plateau value approximately equal to the nominal strength of dogbone specimens (2.4 MPa) tested at a similar strain rate. Similarly, the normalised separation at peak traction δ_{nc}/t increases asymptotically towards a value of approximately 2.0, and the normalised energy dissipation (calculated as the area Γ_n under the traction versus separation response divided by the adhesive layer thickness t) follows a similar path towards an asymptote located at approximately 4.5 MJ/m³. The initial modulus of each joint is plotted in Figure 5(d) along with an analytical prediction as developed by Gent and Lindley (Gent and Lindley, 1959a) for the effective moduli of constrained elastomeric joints of rectangular cross-sections. Good agreement with the analytical curve is observed as the modulus increases sharply with increasing shape factor.

3.2.2 Double-lap Shear Joints

The shear traction T_s versus separation δ_s response of a double-lap shear specimen is shown in Figure 6(a). The dimensions of each adhesive layer are as follows: overlap length $h = 19$ mm, depth $B = 12.8$ mm, and adhesive layer thickness $s = 1.1$ mm. Images and sketches illustrate the observed process of crack growth in Figure 6(b). The response is linear up to point (ii) at a displacement of approximately 2.5 mm. Tensile cracks initiate on free surfaces at locations of high tensile stress⁵. With continued shear displacement, the cracks extend considerably in length with negligible change in shear traction to point (iii). Final failure is by fracture of an entire adhesive layer at point (iv).

⁵ The tensile cracks are associated with the corner singularity, as discussed by Gent (2007).

3.3 Discussion of the Response of Planar Adhesive Joints

Cavitation is predicted to occur for constrained rubber when the hydrostatic stress is equal to $5E/6$ (Green and Zerna 1954). Cavitation was observed in a series of careful experiments by Gent and Lindley (1959). In their study, it was also observed that the knee in the tensile response of a rubber joint becomes more pronounced in more-constrained joints, occurring at higher values of remote stress. The observed T_n - δ_n curves for butt joint specimens in the present study (Figure 4) are consistent with the experimental findings of Gent and Lindley (1959).

When subjected to repeated cycles of loading and unloading, the SMP adhesive displays the “Mullins effect” common to elastomers, whereby the unloading response deviates from the loading response (Mullins, 1969). There is no agreement as to the physical cause of the Mullins effect; various interpretations have been put forward (Diani et al., 2009). The simplest explanation is that crosslinks between polymer chains rupture as they are extended beyond a critical stretch ratio (Blanchard and Parkinson 1952), but this explanation fails to capture the observation of gradual recovery of stiffness for rubber joints which have been stretched and relaxed. Houwink (1956) proposed an alternative theory, suggesting that polymeric chains slip over one another, rather than rupture. The theory relies on a recoverable change in the configurational entropy of polymer chains to explain the observed damage recovery which occurs for stressed specimens which are left at room temperature for a sufficient amount of time. Additional interpretations include rupture of filler material such as carbon-black (Kraus, 1963) and progressive disentanglement of polymer chains (Hanson et al., 2005).

Our observation of void growth in Figure 4(c) and the unloading/re-loading behaviour in Figure 3(b) and Figure 4(b) suggest the following interpretation of the Mullins effect. Upon initial loading, void cavitation occurs at a hydrostatic stress on the order of $5E/6$, see for example the work of Gent and Lindley (1959a) and of Ball (1982). Cavitation gives rise to a significant volume expansion, as measured by Hocine et al (2011), with the matrix responding in an almost incompressible manner (Aït Hocine et al., 2011). A knee in the T - δ curve occurs at the onset of cavitation.

Now consider an unload/re-load cycle as shown in Figure 7(a). The voids close into crack-like features under diminishing load (and become undetectable by the CT scanner). Also, the matrix between voids relaxes from a stretched configuration of molecular alignment back to

the natural state. Upon re-loading, the crack-like features reopen into near-spherical voids and the compliance increases. With continued loading the matrix undergoes orientation-hardening. After the initial loading curve is recovered, additional void growth takes place until a coalescence event leads to rupture. The optical micrograph in Figure 7(b) demonstrates the distribution of voids on the failure surface of a butt joint. The optical micrograph of a single void in Figure 7(c) provides evidence of void growth by tearing.

Now consider the response of the planar double-lap shear joints. Gent, Suh and Kelly (2007) have proposed that cavitation is a possible failure mechanism for a rubber block under shear loading similar to the double-lap shear joints presented in this study. No cavitation is observed in the present experiment. Instead, crack initiation and growth is observed at the location of highest tensile stress along the free edges of each shear region.

4. Results and Discussion for Square-wave Adhesive Joints

Results of tensile tests on butt joints with square-wave interfaces are presented in Figure 8. The square-wave amplitude A was varied in the range 0 mm (corresponding to a planar butt joint) to 20 mm. Two values of adhesive layer thickness t were studied ($t = 1.1$ mm and 4.0 mm). Traction versus displacement responses of square-wave joints are shown in Figure 8(a) and (c) for $t = 1.1$ mm and $t = 4.0$ mm, respectively, and failure sequences of these joints are shown in Figure 8(b) and (d).

Five common events (i) to (v) were observed in the failure sequence of square-wave joints with $t = 1.1$ mm. Their locations are indicated in Figure 8(a), along with sketches to illustrate them in Figure 8(b). The failure sequence occurs as follows. After an initial linear response, void cavitation occurs and the response becomes non-linear. The spherical voids coalesce in the through-thickness direction at each “inside” corner of the square-wave joint and continue to grow as cylindrical voids, event (i). The traction attains a peak value at (ii), and the cylindrical voids coalesce, (iii). Cracks initiate from the corners and extend into the shear regions (iv), until they eventually coalesce, (v). The square-wave joint is still able to bear load, however, due to friction between the failed shear surfaces. The traction drops to zero as opposing shear surfaces separate.

Square-wave joints of thickness $t = 4.0$ mm exhibited a different failure sequence: see Figure 8(c), with sketches and photographs in Figure 8(d). The failure sequence for these joints is as

follows. Void cavitation occurs after an initial linear response, and spherical voids coalesce at each inside square-wave corner to form through-thickness cylindrical voids (i). The cylindrical voids experience stable growth into tensile regions, and significant crack growth occurs simultaneously in the shear regions (ii). After the remote traction attains a peak value, crack growth causes failure in one or more shear regions (iii). The tensile regions fail shortly thereafter (iv), and the traction drops to zero as opposing shear surfaces are drawn apart.

Higher values of peak traction and energy dissipation are observed for all tested square-wave joints compared to planar joints. While planar joints fail by cavitation and the growth of spherical voids, square-wave joints fail in a complex but repeatable sequence involving the formation and propagation of through-thickness cylindrical voids at each corner. Shear regions fail before the tensile regions in square-wave joints of thickness $t = 1.1$ mm, while this order of events is reversed in square-wave joints of thickness $t = 4.0$ mm. It is clear that the square-wave joint offers the opportunity for optimisation of strength and toughness. This is explored more fully in the next section.

5. Modelling the Response of a Square-wave Joint

5.1 Superposition Model

Representative traction versus separation responses of a butt joint and a double-lap shear joint are used to construct a “superposition model” of the behaviour of a square-wave joint in Figure 9. Each tensile region in the square-wave joint (marked (n) in Figure 1) is approximated as a tensile butt joint and each shear region (marked (s) in Figure 1) as half of a double-lap shear joint.

It is observed in Figure 9 that the predicted peak strength associated with failure of the tensile regions of the square-wave specimen exceeds the observed peak strength by 45%. Furthermore, the predicted failure of tensile regions in the square-wave joint occurs at a displacement of 2.1 mm, which exceeds the measured value of 1.4 mm. The second peak stress corresponds to failure of the shear regions of the square-wave joint; for the second failure event, both the predicted strength and failure displacement are below the observed values.

Additional predictions for each of the four square-wave joint geometries are given in Figure 10; in this figure the measured and predicted square-wave responses are compared. Two

parameters are explored: The peak traction \hat{T}_c is plotted as a function of amplitude A for (a) $t = 1.1$ mm and (b) $t = 4.0$ mm, and the energy dissipated within the joint $\hat{\Gamma}$ is plotted against A for (c) $t = 1.1$ mm and (d) $t = 4.0$ mm. The superposition model over-predicts the peak traction of square-wave joints, whereas the predicted dissipation is in adequate agreement with the measured values. In broad terms, the superposition model captures the increase in $(\hat{T}_c, \hat{\Gamma})$ with increasing A .

5.2 Idealised Model

An additional “idealised model” is now developed. It assumes rectangular and triangular traction versus separation responses for tensile and shear regions, respectively; see Figure 11. The rectangular, tensile traction versus separation law is characterised by a peak traction T_{nc} and an energy dissipation Γ_n , and the triangular, shear traction-separation law is likewise characterised by a peak traction T_{sc} and an energy dissipation Γ_s . The critical displacements follow immediately: the critical tensile opening δ_{nc} equals Γ_n/T_{nc} and the critical shear displacement δ_{sc} equals $2\Gamma_s/T_{sc}$.

Based on the simple model presented in Figure 11, the traction versus displacement response of a square-wave joint can take three general forms. Consider first the case where the tensile regions fail before shear regions, i.e. $\delta_{sc}/\delta_{nc} > 1$. Then, the square-wave response can take one of the forms as described by Figure 12(a) and Figure 12(b). If the peak load occurs when the tensile region fails, (a “Type I” failure), then the peak traction reads

$$\hat{T}_{c_1} = \frac{2}{\lambda} \left[T_{nc}w + T_{sc}(A - t) \left(\frac{\delta_{nc}}{\delta_{sc}} \right) \right] \quad (2)$$

where the shear overlap h is expressed as $A - t$. Alternatively, if the peak traction occurs when the shear region fails (a so-called “Type II” failure), then the peak traction reads

$$\hat{T}_{c_2} = \frac{2}{\lambda} T_{sc}(A - t) \quad (3)$$

The transition between these two types occurs at

$$\frac{T_{nc}}{T_{sc}} = \frac{(A - t)}{w} \left(1 - \frac{\delta_{nc}}{\delta_{sc}} \right) \quad (4)$$

Second, consider the case where the shear regions fail before the tensile regions, i.e. $\delta_{sc}/\delta_{nc} < 1$, and refer to this as a ‘‘Type III’’ failure. The peak traction is given by

$$\hat{T}_{c_3} = \frac{2}{\lambda} [T_{nc}w + T_{sc}(A - t)] \quad (5)$$

The full expression for the peak traction of a square-wave joint is thus

$$\hat{T}_c = \begin{cases} \max\{\hat{T}_{c_1}, \hat{T}_{c_2}\} & , \quad \frac{\delta_{sc}}{\delta_{nc}} \geq 1 \\ \hat{T}_{c_3} & , \quad \frac{\delta_{sc}}{\delta_{nc}} < 1 \end{cases} \quad (6)$$

The predicted toughness of a square-wave joint is more straightforward. It is calculated as a simple sum of the energy dissipated by tensile and shear regions.

$$\hat{\Gamma} = \frac{2}{\lambda} [\Gamma_n w + \Gamma_s (A - t)] \quad (7)$$

As for the ‘‘superposition model,’’ the behaviour of the idealised model is explored in Figure 10. The peak traction \hat{T}_c is plotted as a function of amplitude A for (a) $t = 1.1$ mm and (b) $t = 4.0$ mm, and the energy dissipated within the joint $\hat{\Gamma}$ is plotted against A for (c) $t = 1.1$ mm and (d) $t = 4.0$ mm. The observed failure is of Type I for $t = 1.1$ mm and of Type III for $t = 4.0$ mm, as predicted by the idealised model. The idealised model again over-predicts the peak traction of square-wave joints, whereas, once again, the predicted dissipation is in adequate agreement with the measured values. As for the superposition model, the idealised model captures the increase in $(\hat{T}_c, \hat{\Gamma})$ with increasing A .

5.3 Development of a Design Map

5.3.1 Strength and Toughness

The strength and toughness of the square-wave joint can now be optimised in terms of its shape and the material properties of the adhesive layer. For illustration purposes, attention is limited to the case of a thin adhesive layer such that $t \ll A$ and $s \ll \lambda$. The strength \hat{T}_c of a square-wave joint is normalised by the strength T_{nc} of a planar joint, such that (2), (3) and (4) become

$$\frac{\hat{T}_{c1}}{T_{nc}} = 1 + \frac{2A}{\lambda} \frac{T_{sc}}{T_{nc}} \left(\frac{\delta_{nc}}{\delta_{sc}} \right) \quad (8)$$

$$\frac{\hat{T}_{c2}}{T_{nc}} = \frac{2A}{\lambda} \frac{T_{sc}}{T_{nc}} \quad (9)$$

and

$$\frac{\hat{T}_{c3}}{T_{nc}} = 1 + \frac{2A}{\lambda} \frac{T_{sc}}{T_{nc}} \quad (10)$$

The active failure mode is again dictated by (6), and the regimes of dominance of Type I, II and III are plotted in Figure 13(a) in terms of the two independent non-dimensional groups δ_{sc}/δ_{nc} and $T_{sc}/T_{nc}(2A/\lambda)$ which arise in (8), (9) and (10). Examination of these expressions reveals that \hat{T}_c/T_{nc} is maximised by taking a large value for $T_{sc}/T_{nc}(2A/\lambda)$.

The toughness of the square-wave joint follows directly from (7) to read

$$\frac{\hat{\Gamma}}{\Gamma_n} = 1 + \frac{A}{\lambda} \frac{T_{sc}}{T_{nc}} \left(\frac{\delta_{sc}}{\delta_{nc}} \right) \quad (11)$$

and this remains valid for all three regimes of tensile failure.

The toughness $\hat{\Gamma}/\Gamma_n$ is maximised by taking large positive values for δ_{sc}/δ_{nc} and $T_{sc}/T_{nc}(2A/\lambda)$, such that the maximum value of $\hat{\Gamma}/\Gamma_n$ is in the top-right corner of the map in Figure 13(a).

5.3.2 Damage Tolerance

The damage tolerance of the square-wave joint is now defined in terms of a transition flaw size \hat{a} as follows. Assume that the square-wave joint contains a macroscopic flaw of length a that spans multiple wavelengths such that $a \gg \lambda$. For a sufficiently large a , the tensile failure strength \hat{T}_f is dictated by the toughness $\hat{\Gamma}$ such that

$$\hat{T}_f = \left(\frac{E\hat{\Gamma}}{\pi a} \right)^{1/2} \quad (12)$$

as given by the usual result for linear elastic fracture mechanics. In contrast, when $a \ll \lambda$, the strength is given by $\hat{T}_f \approx \hat{T}_c$.

By equating the two expressions (11) and (12), a value for the transition flaw size is obtained as

$$\hat{a} = \frac{1}{\pi} \frac{E\hat{\Gamma}}{\hat{T}_c^2} \quad (13)$$

This flaw size is interpreted as a characteristic property of the joint, and referred to as the ‘damage tolerance’ of the joint. The value of \hat{a} is dependent upon the tensile failure type I, II or III as defined in Figure 12. It is convenient to normalise \hat{a} by the value a_n for a planar joint where

$$a_n = \frac{1}{\pi} \frac{E\Gamma_n}{T_{nc}^2} \quad (14)$$

The normalised transition flaw size \hat{a}/a_n is thus

$$\frac{\hat{a}}{a_n} = \frac{\hat{\Gamma}/\Gamma_n}{(\hat{T}_c/T_{nc})^2} \quad (15)$$

Now plot contours of \hat{T}_c/T_{nc} , $\hat{\Gamma}/\Gamma_n$ and \hat{a}/a_n on the design map: see Figure 13(b). The regime of optimal \hat{a}/a_n exists at high values of δ_{sc}/δ_{nc} and intermediate values of $T_{sc}/T_{nc}(2A/\lambda)$, as shown on the map. It is noted that the optimal values of strength, toughness and damage tolerance occupy different regions of the map.

6. Concluding Remarks

The traction versus separation responses of square-wave butt joints are explained in terms of the observed failure mechanisms. The square-wave joint behaves as a combination of a planar butt joint and a lap shear joint. For a given adhesive layer thickness, the peak strength and energy dissipation increase with joint amplitude A , but with a penalty associated with stress concentrations at square-wave corners. These results demonstrate that the strength of a rubber-like adhesive joint can be elevated well beyond the critical pressure for cavitation ($P_c = 5E/6$) as first proposed by Gent and Lindley (1959).

A design map for square-wave joints is presented which assumes a rectangular traction versus separation response in tensile regions and a triangular traction versus separation response in shear regions. It is demonstrated that the ideal geometry for maximising strength differs from the ideal geometry for toughness or damage tolerance.

7. Acknowledgements

The authors gratefully acknowledge financial support for this research received from the Materials Innovation Institute (www.M2i.nl) and Damen Schelde Naval Shipbuilding.

8. References

- Aït Hocine, N., Hamdi, A., Naït Abdelaziz, M., Heuillet, P., Zaïri, F., 2011. Experimental and finite element investigation of void nucleation in rubber-like materials. *Int. J. Solids Struct.* 48, 1248–1254. doi:10.1016/j.ijsolstr.2011.01.009
- Ball, J.M., 1982. Discontinuous Equilibrium Solutions and Cavitation for Nonlinear Elasticity. *Philos. Trans. R. Soc. London. Ser. A, Math. Phys. Sci.* 306.
- Blanchard, A.F., Parkinson, D., 1952. Breakage of Carbon-Rubber Networks by Applied Stress. *Ind. Eng. Chem.* 44, 799–812. doi:10.1021/ie50508a034
- Boyd, S.W., Dulieu-Barton, J.M., Rumsey, L., 2006. Stress analysis of finger joints in pultruded GRP materials. *Int. J. Adhes. Adhes.* 26, 498–510. doi:10.1016/j.ijadhadh.2005.07.003
- Cordisco, F.A., Zavattieri, P.D., Hector, L.G., Carlson, B.E., 2016. Mode I fracture along adhesively bonded sinusoidal interfaces. *Int. J. Solids Struct.* 83, 45–64. doi:10.1016/j.ijsolstr.2015.12.028
- Diani, J., Fayolle, B., Gilormini, P., 2009. A review on the Mullins effect. *Eur. Polym. J.* 45, 601–612. doi:10.1016/j.eurpolymj.2008.11.017
- Gent, A.N., Lindley, P.B., 1959a. The Compression of Bonded Rubber Blocks. *Proc Instn Mech Engrs* 173. doi:10.5254/1.3547824
- Gent, A.N., Lindley, P.B., 1959b. Internal rupture of bonded rubber cylinders in tension. *Proc. R. Soc. London* 249, 195–205.

- Gent, A.N., Suh, J.B., Kelly, S.G., 2007. Mechanics of rubber shear springs. *Int. J. Non-Linear Mech.* 42, 241–249. doi:10.1016/j.ijnonlinmec.2006.11.006
- Green, A.E., Zerna, W., 1954. *Theoretical elasticity*. Oxford University Press.
- Haghpanah, B., Chiu, S., Vaziri, A., 2014. Adhesively bonded lap joints with extreme interface geometry. *Int. J. Adhes. Adhes.* 48, 130–138. doi:10.1016/j.ijadhadh.2013.09.041
- Hanson, D.E., Hawley, M., Houlton, R., Chitanvis, K., Rae, P., Orlor, E.B., Wroblewski, D.A., 2005. Stress softening experiments in silica-filled polydimethylsiloxane provide insight into a mechanism for the Mullins effect. *Polymer (Guildf)*. 46, 1–6. doi:10.1016/j.polymer.2005.09.039
- Hattori, R., Takei, K., 1950. Spring constants of compressive rubber blocks. *J. Soc. Rubber Ind. Japan* 23, 194–198.
- Houwink, R., 1956. Slipping of Molecules during the Deformation of Reinforced Rubber. *Rubber Chem. Technol.* doi:10.5254/1.3542602
- Kraus, G., 1963. Swelling of filler-reinforced vulcanizates. *J. Appl. Polym. Sci.* 7, 861–871. doi:10.1002/app.1963.070070306
- Li, Y., Ortiz, C., Boyce, M.C., 2012. Bioinspired, mechanical, deterministic fractal model for hierarchical suture joints. *Phys. Rev. E - Stat. Nonlinear, Soft Matter Phys.* 85, 1–14. doi:10.1103/PhysRevE.85.031901
- Li, Y., Ortiz, C., Boyce, M.C., 2011. Stiffness and strength of suture joints in nature. *Phys. Rev. E* 84, 62904. doi:10.1103/PhysRevE.84.062904
- Mullins, L., 1969. Softening of Rubber by Deformation. *Rubber Chem. Technol.* doi:10.5254/1.3539210
- Reedy, E.D., Moody, N.R., Zimmerman, J.A., Zhou, X., Kennedy, M.S., Mook, W.M., Bahr, D.F., 2007. Effect of Nanoscale Patterned Interfacial Roughness on Interfacial Toughness.
- Suzuki, T., Matsuzaki, R., Todoroki, A., Mizutani, Y., 2013. Crack growth analysis of a composite/adhesive interface toughened by in-mold surface preparation. *Int. J. Adhes. Adhes.* 42, 36–43. doi:10.1016/j.ijadhadh.2013.01.008
- Zavattieri, P.D., Hector, L.G., Bower, A.F., 2007. Determination of the effective mode-I

toughness of a sinusoidal interface between two elastic solids. Int. J. Fract. 145, 167–180. doi:10.1007/s10704-007-9109-y

9. Tables

t	s	A	λ	w	h	b
1.1 – 4.0	1.1	0 – 20	28.0	12.9	8.9 – 18.9	25.4

Table 1: Dimensions of square-wave joints. Measurement uncertainty is equal to ± 0.1 mm except where otherwise specified. All dimensions in millimetres, measured prior to testing. Depth B (into page) for all specimens is 12.8 ± 0.2 mm.

Test Geometry	t	s	w	h	b	B
Dogbone	--	--	6.5	20.0	--	6.5
Butt joint	1.1 – 4.0	--	13 – 50	--	40	12.8
Double-lap shear	--	1.1	13.0	9.0 – 19.0	40 – 70	12.8

Table 2: Average dimensions of planar test geometries. All dimensions in millimetres, measured prior to testing. Measurement uncertainty is equal to ± 0.1 mm except where otherwise specified.

Test Geometry	t, h	K	T_{nc}, T_{sc}	Γ_n, Γ_s	$\delta_{nc}/t, \delta_{sc}/s$
	mm	MPa/mm	MPa	kJ/m^2	--
Butt joint	$t = 1.1 \pm 0.1$	18 ± 3	2.2 ± 0.1	3.6 ± 0.9	1.7 ± 0.3

Butt joint	$t = 4.0 \pm 0.2$	1.6 ± 0.2	2.0 ± 0.2	11 ± 2	1.5 ± 0.2
Double-lap shear	$h = 9.0 \pm 0.1$	0.9 ± 0.1	2.3 ± 0.1	6.0 ± 0.7	3.0 ± 0.3
Double-lap shear	$h = 19.0 \pm 0.1$	0.8 ± 0.1	1.8 ± 0.1	4.9 ± 0.3	2.6 ± 0.2
Table 3: Stiffness K, peak traction T_{nc} and T_{sc}, energy dissipation Γ_n and Γ_s and normalised displacement at peak traction δ_{nc}/t and δ_{sc}/s of butt joints and double-lap shear specimens.					

A	t	K	\hat{T}_c	$\hat{\Gamma}$	$\hat{\delta}_c/t$
<i>mm</i>	<i>mm</i>	<i>MPa/mm</i>	<i>MPa</i>	<i>kJ/m²</i>	--
10.0	1.1 ± 0.1	12 ± 1	2.4 ± 0.1	6.5 ± 0.9	1.4 ± 0.3
20.0	1.1 ± 0.1	13 ± 1	2.9 ± 0.2	12.7 ± 0.6	1.2 ± 0.2
10.0	4.0 ± 0.2	3.1 ± 0.2	2.2 ± 0.3	8 ± 2	0.70 ± 0.09
20.0	4.0 ± 0.2	3.0 ± 0.5	3.3 ± 0.3	14 ± 2	0.75 ± 0.09
Table 4: Stiffness K, peak traction \hat{T}_c, energy dissipation $\hat{\Gamma}$ and normalised displacement at peak traction $\hat{\delta}_c/t$ of square-wave joints.					

10. List of Figure Captions

Figure 1: A unit cell of the square-wave joint. The encircled letters refer to portions of the adhesive layer that are subjected to different regimes of stress state. Depth (into page) is $B = 12.8$ mm.

Figure 2: (a) Dogbone tensile specimen; (b) butt joint; (c) double-lap shear joint; (d) square-wave tensile specimen. Depth (into page) of all specimens is $B = 12.8$ mm.

Figure 3: (a) Uniaxial tension response of silyl-modified polymer (SMP) adhesive at three strain rates, from dogbone specimens. (b) Unloading curves as observed in a dogbone specimen.

Figure 4: (a) The effect of constraint on the traction versus normalised separation response of butt joints of SMP adhesive. (b) Traction versus separation response of butt joint (adhesive layer thickness $t = 1.1$ mm, width $w = 13.0$ mm, depth $B = 12.8$ mm, $S = 2.9$); (c) CT images of planes P_1 , P_2 , and P_3 at four loading points (i) to (iv), and failure surface (v). Each plane and loading point is indicated in (b).

Figure 5: The relationship between shape factor S and (a) peak normal traction T_{nc} , (b) normalised energy dissipation Γ_n/t , (c) normalised displacement at peak traction δ_{nc}/t and (d) joint modulus E^*/E for butt joints of SMP adhesive. Results are presented for two adhesive layer thicknesses $t = 1.1 \pm 0.1$ mm and $t = 4.0 \pm 0.2$ mm.

Figure 6: (a) Shear traction versus separation response of a double-lap shear specimen. Depth (into page) $B = 12.8$ mm. (b) A sketch of crack initiation and growth.

Figure 7: (a) Proposed mechanics of the Mullins effect during one un-load/reload cycle. (b) Optical micrograph showing a distribution of voids of the failure surface of a butt joint (adhesive layer thickness $t = 1.1$ mm). (c) Optical micrograph of a torn void in the failure surface of a butt joint (adhesive layer thickness $t = 4.0$ mm).

Figure 8: (a) Traction versus separation responses of two square-wave joints with different amplitudes ($t = 1.1 \pm 0.1$ mm, $A = 10$ and 20 mm) compared against a planar butt joint, $t = 1.1$ mm, $w = 13$ mm, $B = 12.8$ mm. (b) Sketches and images show failure sequence of a square-wave joint with adhesive layer thickness $t = 1.1$ mm. (c) Traction versus separation curves for two square-wave joints with thicker tensile regions ($t = 4.0 \pm 0.2$ mm, $A = 10$ and

20 mm) and a planar butt joint, $t = 4.0$ mm, $w = 13$ mm, $B = 12.8$ mm. (d) Sketches and photos of failure sequence.

Figure 9. Traction versus separation responses of a butt joint (dashed line; $t = 1.1$ mm, $w = 13$ mm, $B = 12.8$ mm) and a double-lap shear joint (dotted line; $s = 1.1$ mm, $h = 19$ mm, $B = 12.8$ mm) are summed (dot-dash line) to predict the response of a square-wave joint (solid line; $A = 20$ mm, $t = 1.1$ mm).

Figure 10. Sensitivity of measured and predicted square-wave responses to amplitude A . Peak traction for (a) $t = 1.1$ mm and (b) $t = 4.0$ mm and energy dissipation for (c) $t = 1.1$ mm and (d) $t = 4.0$ mm.

Figure 11. A square-wave joint can be approximated as a simple sum of tensile and shear regions. The model assumes a rectangular traction-separation law for tensile regions and a triangular law for shear regions.

Figure 12. Superposition of simplified tensile and shear contributions imply three types of possible responses for a square-wave joint: (a) Type I, (b) Type II and (c) Type III. The three possible peak traction values are indicated.

Figure 13. (a) Three regimes of square-wave behaviour are identified. (b) Contours of normalised square-wave traction, energy dissipation and transition flaw size illustrate the available property space for square-wave joints.

Figures

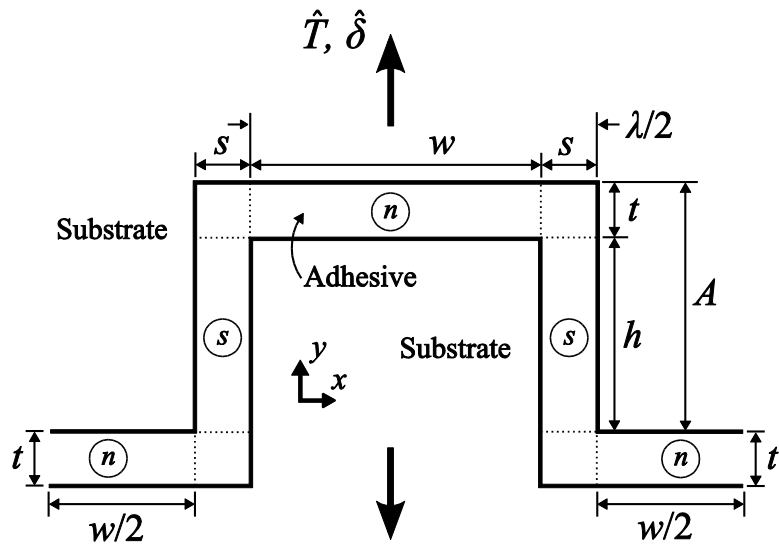


Figure 1: A unit cell of the square-wave joint. The encircled letters refer to portions of the adhesive layer that are subjected to different regimes of stress state. Depth (into page) is $B = 12.8$ mm.

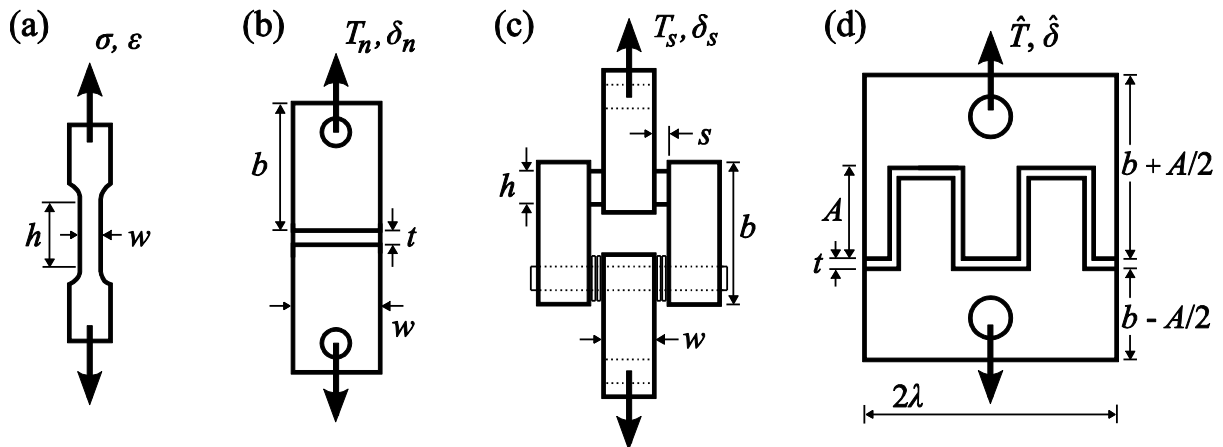


Figure 2: (a) Dogbone tensile specimen; (b) butt joint; (c) double-lap shear joint; (d) square-wave tensile specimen. Depth (into page) of all specimens is $B = 12.8$ mm.

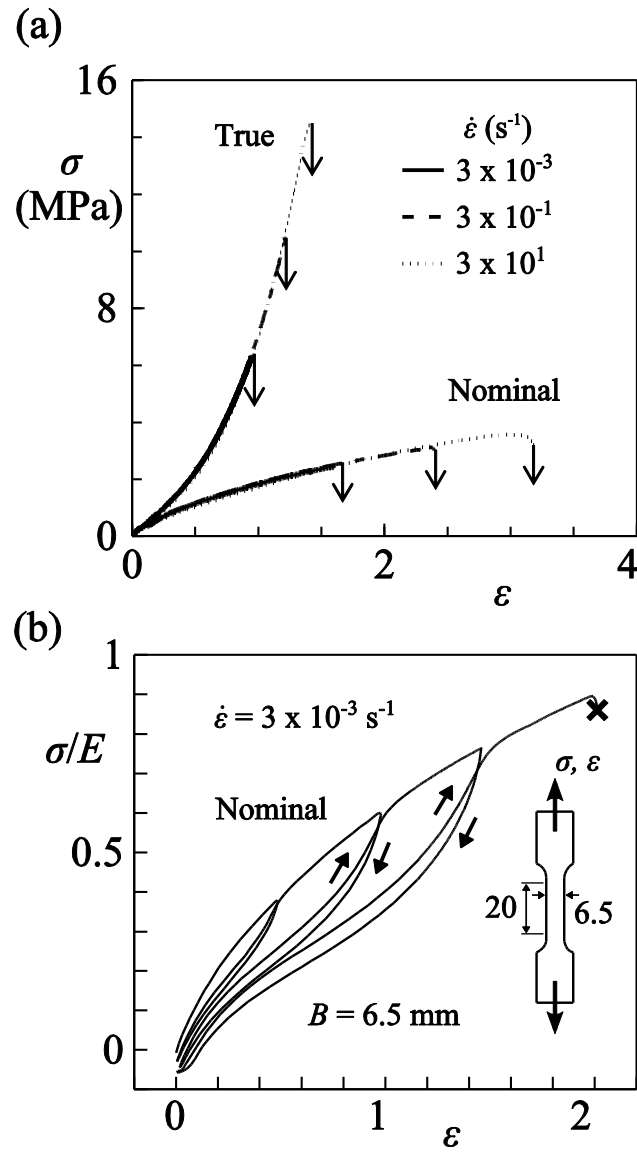


Figure 3: (a) Uniaxial tension response of silyl-modified polymer (SMP) adhesive at three strain rates, from dogbone specimens. (b) Unloading curves as observed in a dogbone specimen.

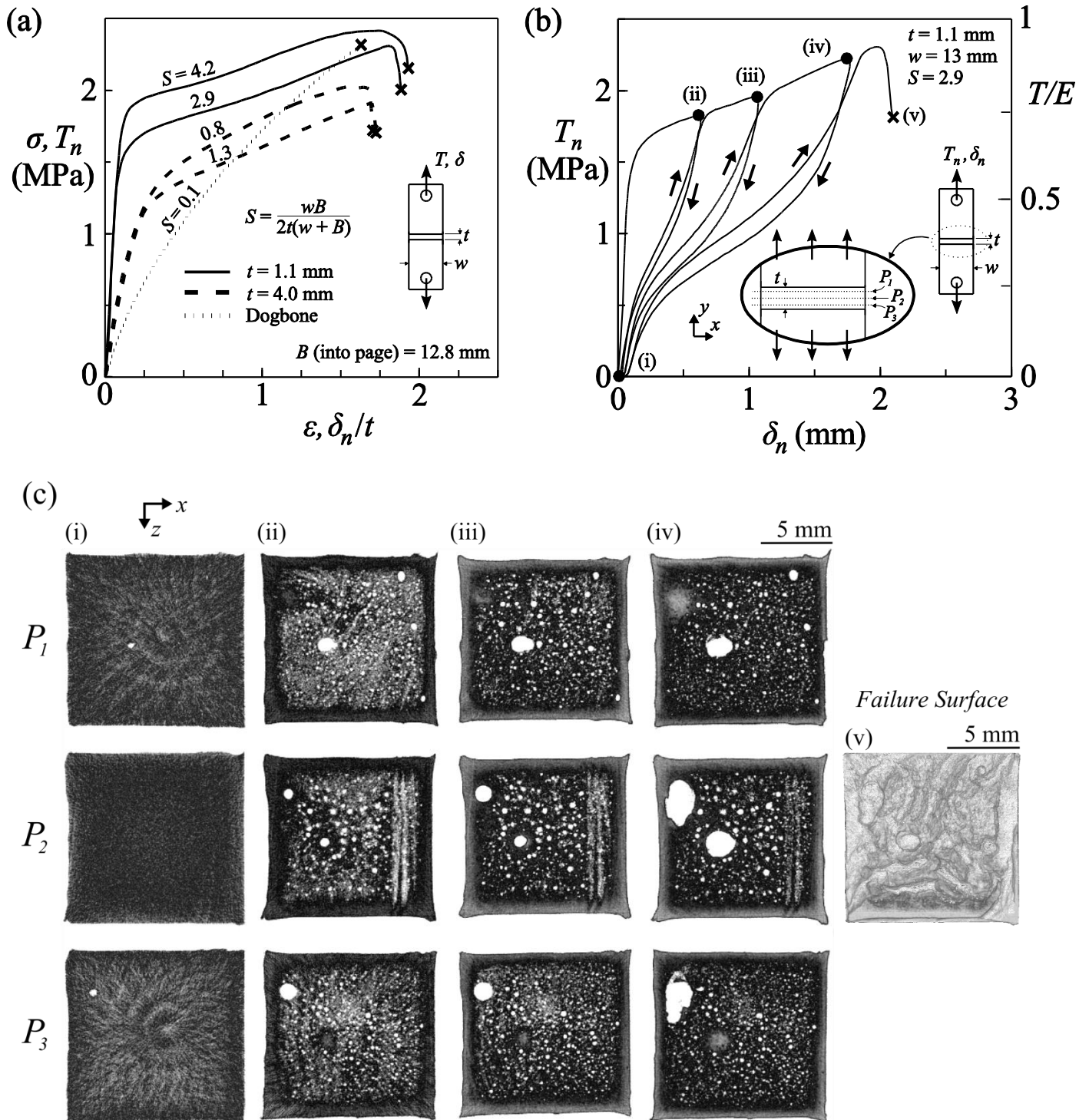


Figure 4: (a) The effect of constraint on the traction versus normalised separation response of butt joints of SMP adhesive. (b) Traction versus separation response of butt joint (adhesive layer thickness $t = 1.1$ mm, width $w = 13.0$ mm, depth $B = 12.8$ mm, $S = 2.9$); (c) CT images of planes P_1, P_2 , and P_3 at four loading points (i) to (iv), and failure surface (v). Each plane and loading point is indicated in (b).

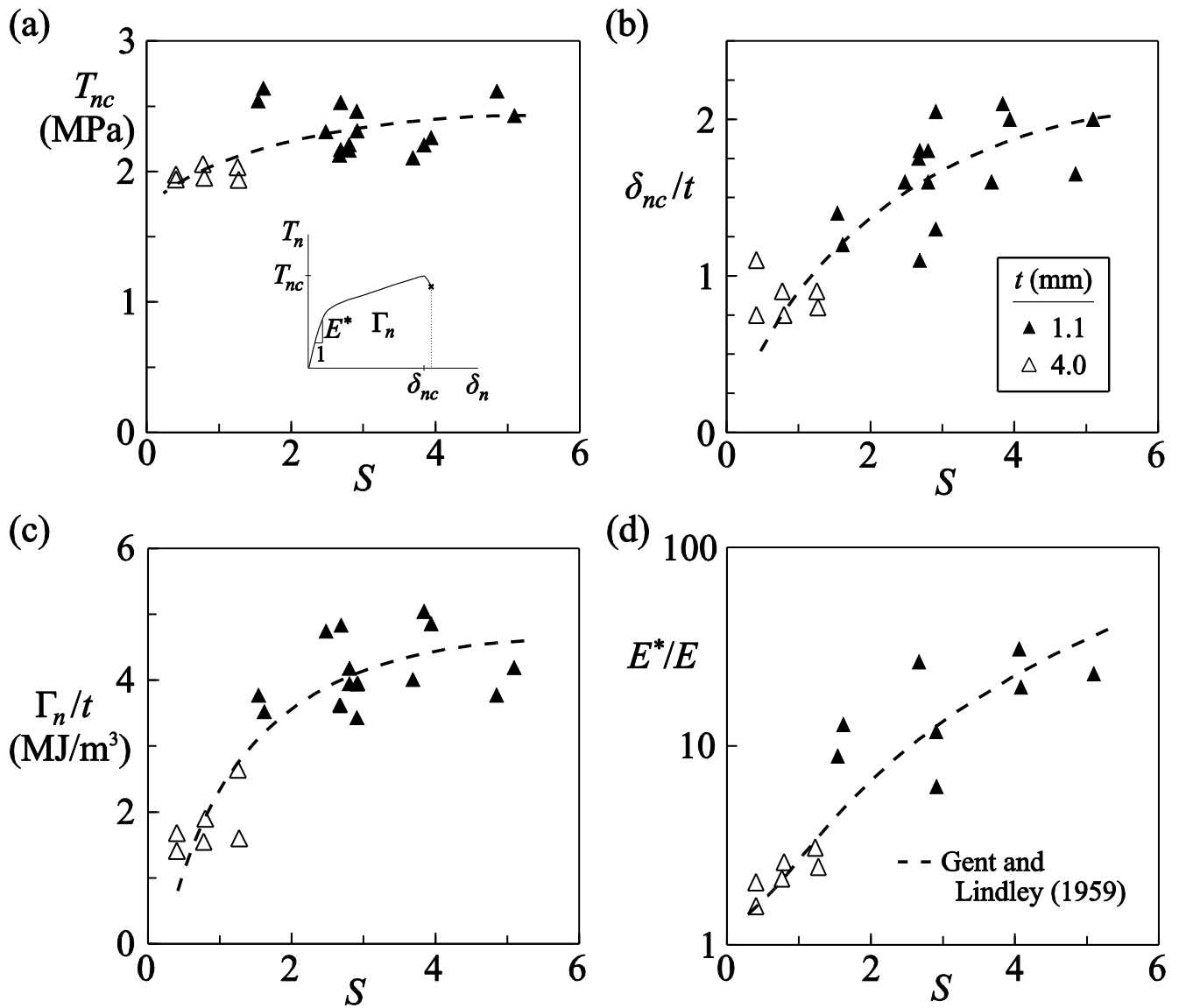


Figure 5: The relationship between shape factor S and (a) peak normal traction T_{nc} , (b) normalised energy dissipation Γ_n/t , (c) normalised displacement at peak traction δ_{nc}/t and (d) normalised joint modulus E^*/E for butt joints of SMP adhesive. Results are presented for two adhesive layer thicknesses $t = 1.1 \pm 0.1$ mm and $t = 4.0 \pm 0.2$ mm.

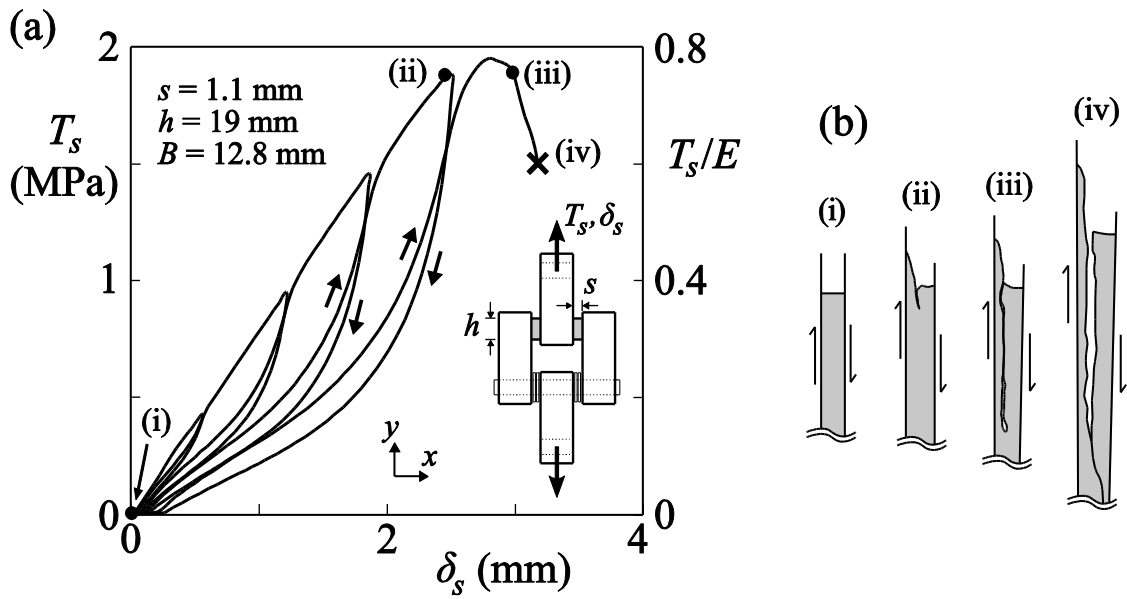


Figure 6: (a) Shear traction versus separation response of a double-lap shear specimen. Depth (into page) $B = 12.8$ mm. (b) A sketch of crack initiation and growth.

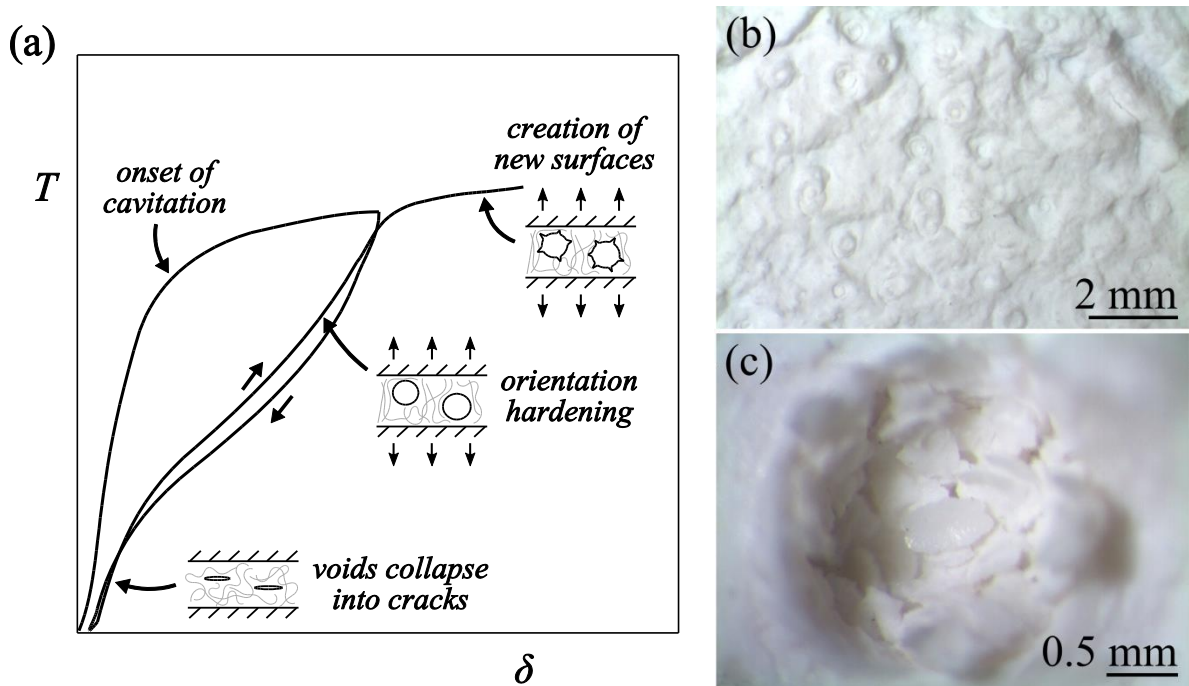


Figure 7: (a) Proposed mechanics of the Mullins effect during one un-load/reload cycle. (b) Optical micrograph showing a distribution of voids of the failure surface of a butt joint (adhesive layer thickness $t = 1.1$ mm). (c) Optical micrograph of a torn void in the failure surface of a butt joint (adhesive layer thickness $t = 4.0$ mm).

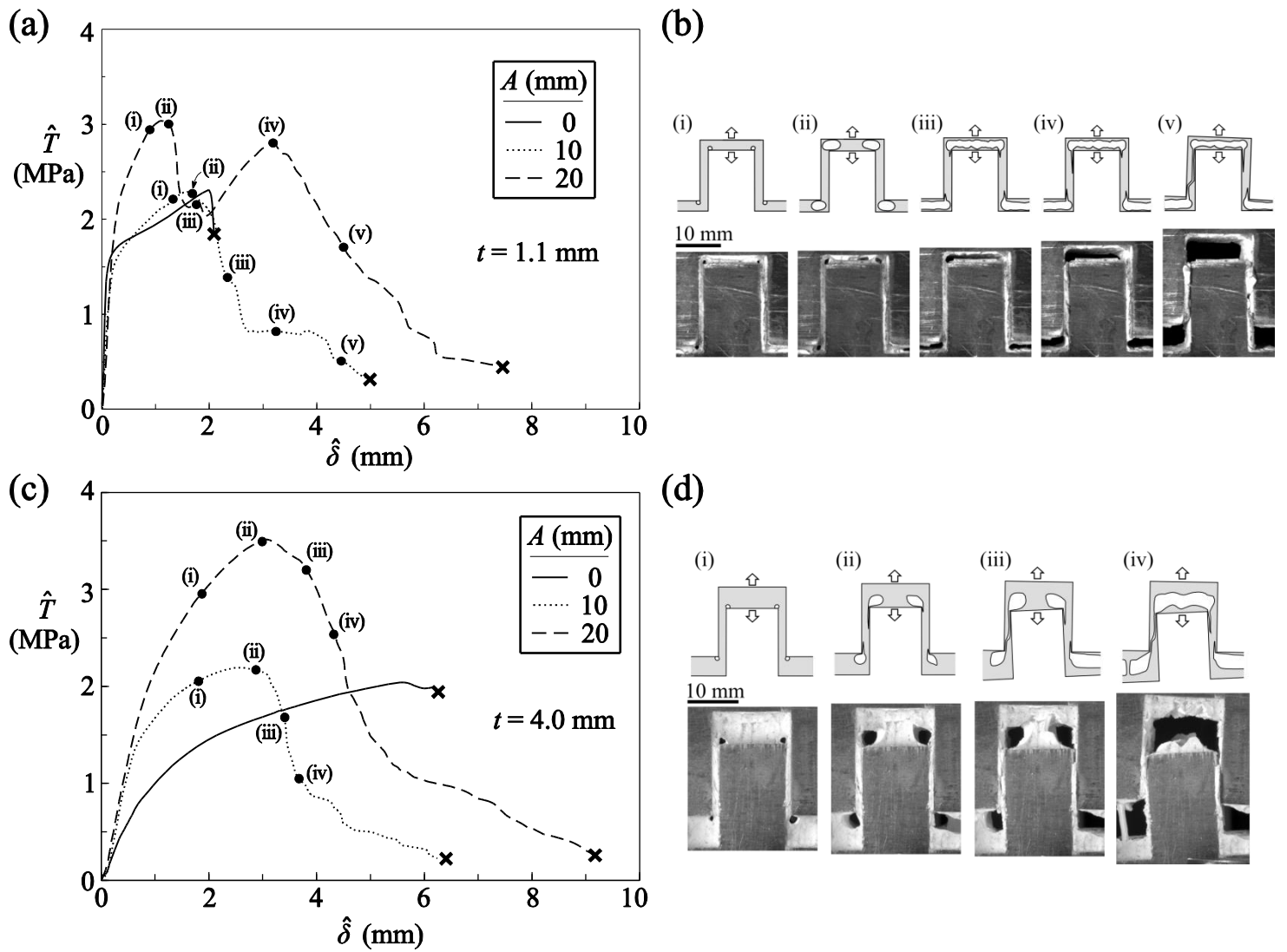


Figure 8: (a) Traction versus separation responses of two square-wave joints with different amplitudes ($t = 1.1 \pm 0.1$ mm, $A = 10$ and 20 mm) compared against a planar butt joint, $t = 1.1$ mm, $w = 13$ mm, $B = 12.8$ mm. (b) Sketches and images show failure sequence of a square-wave joint with adhesive layer thickness $t = 1.1$ mm. (c) Traction versus separation curves for two square-wave joints with thicker tensile regions ($t = 4.0 \pm 0.2$ mm, $A = 10$ and 20 mm) and a planar butt joint, $t = 4.0$ mm, $w = 13$ mm, $B = 12.8$ mm. (d) Sketches and photos of failure sequence.

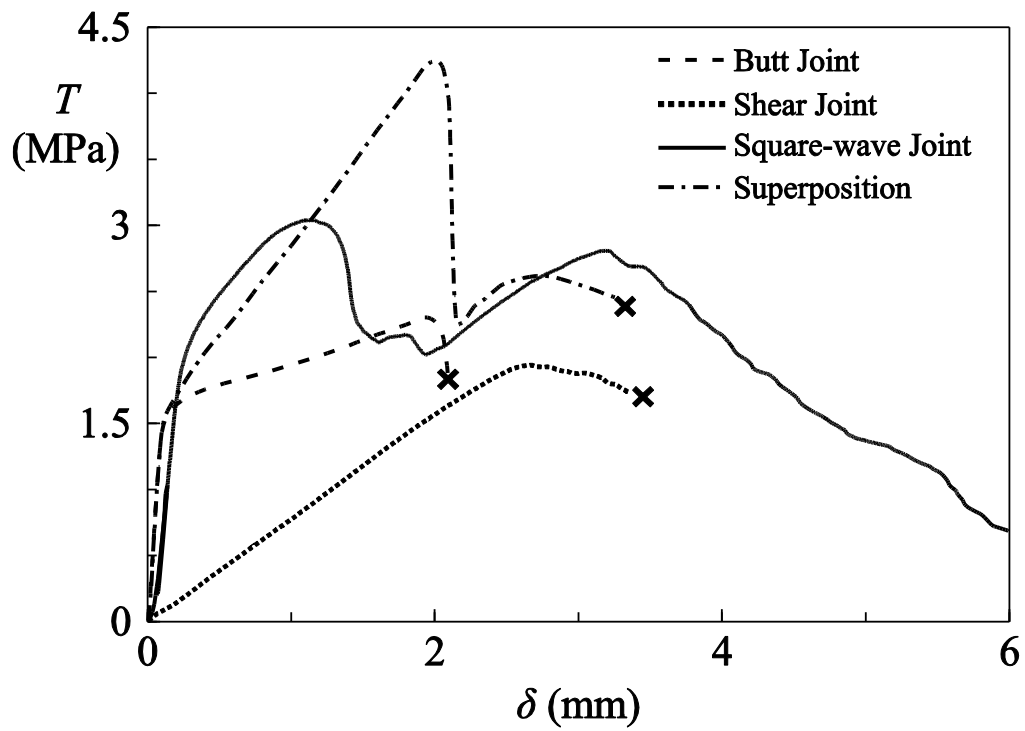


Figure 9. Traction versus separation responses of a butt joint (dashed line; $t = 1.1$ mm, $w = 13$ mm, $B = 12.8$ mm) and a double-lap shear joint (dotted line; $s = 1.1$ mm, $h = 19$ mm, $B = 12.8$ mm) are summed (dot-dash line) to predict the response of a square-wave joint (solid line; $A = 20$ mm, $t = 1.1$ mm).

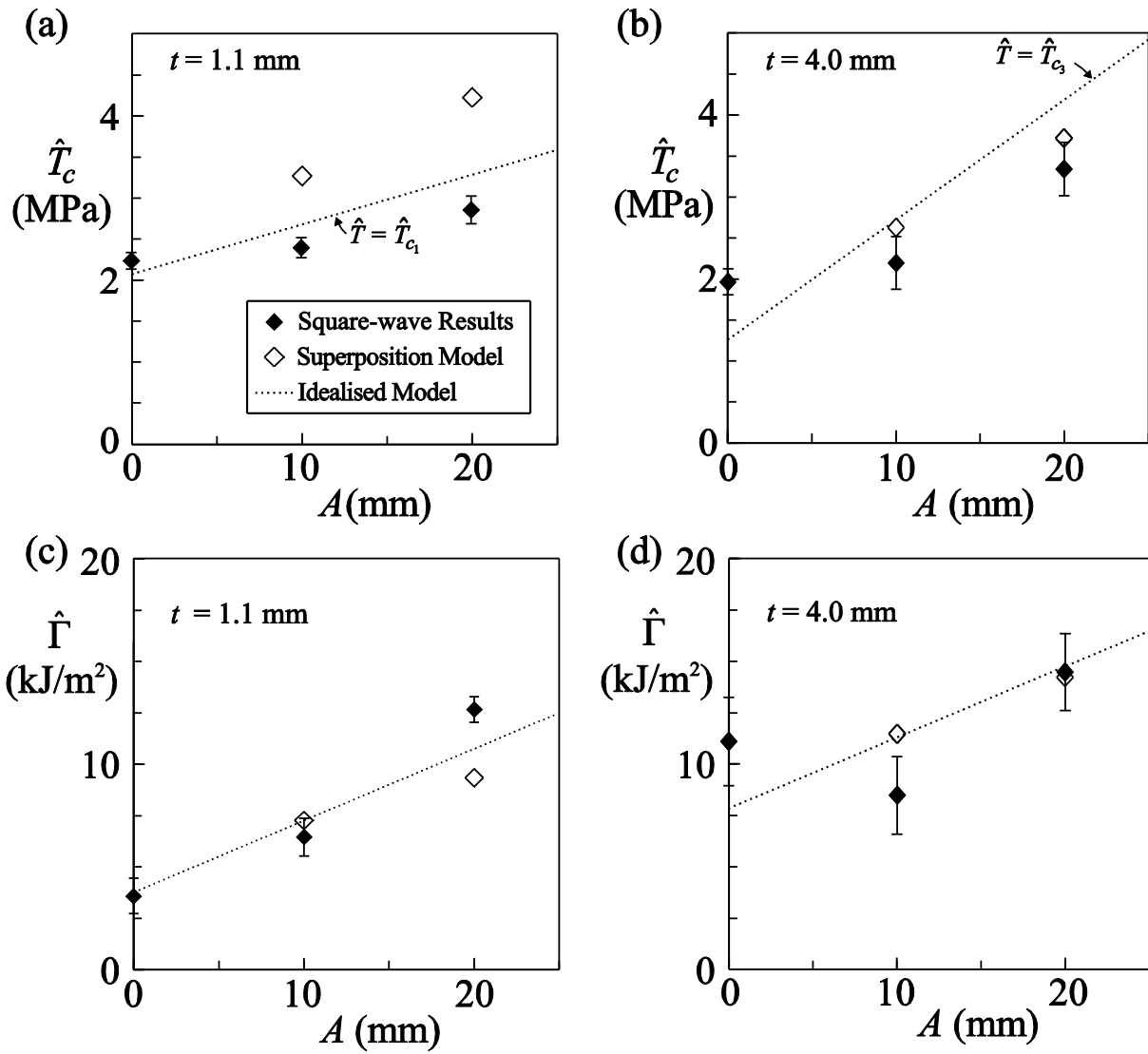


Figure 10. Sensitivity of measured and predicted square-wave responses to amplitude A . Peak traction for (a) $t = 1.1$ mm and (b) $t = 4.0$ mm and energy dissipation for (c) $t = 1.1$ mm and (d) $t = 4.0$ mm.

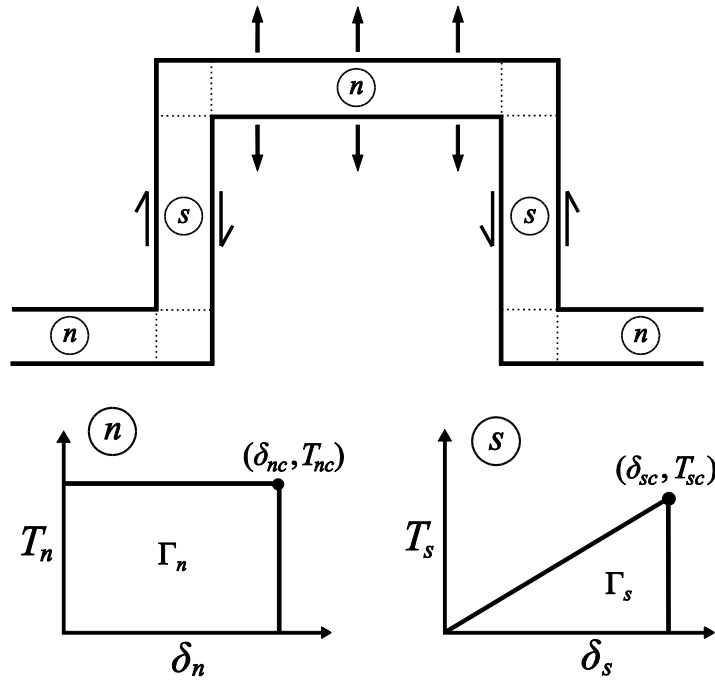


Figure 11. A square-wave joint can be approximated as a simple sum of tensile and shear regions. The model assumes a rectangular traction-separation law for tensile regions and a triangular law for shear regions.

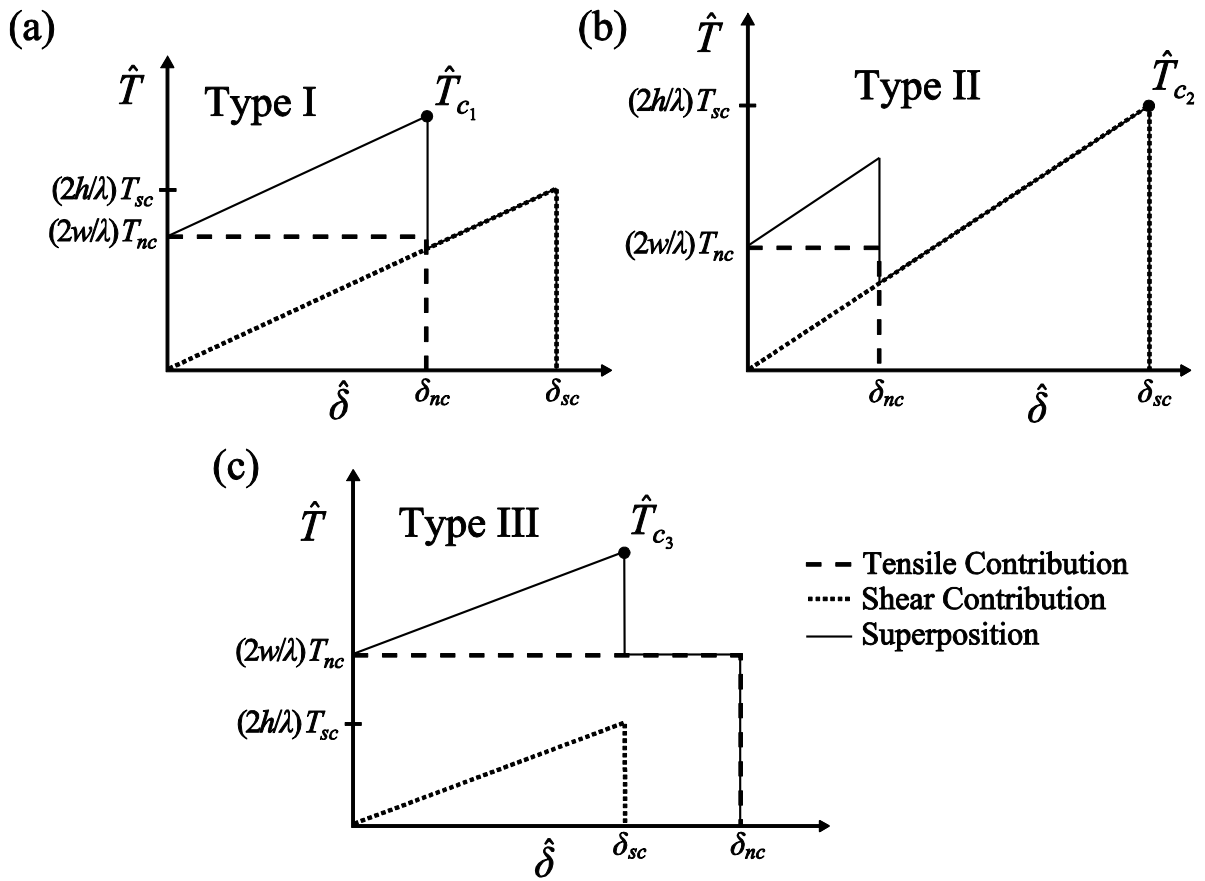


Figure 12. Superposition of simplified tensile and shear contributions imply three types of possible responses for a square-wave joint: (a) Type I, (b) Type II and (c) Type III. The three possible peak traction values are indicated.

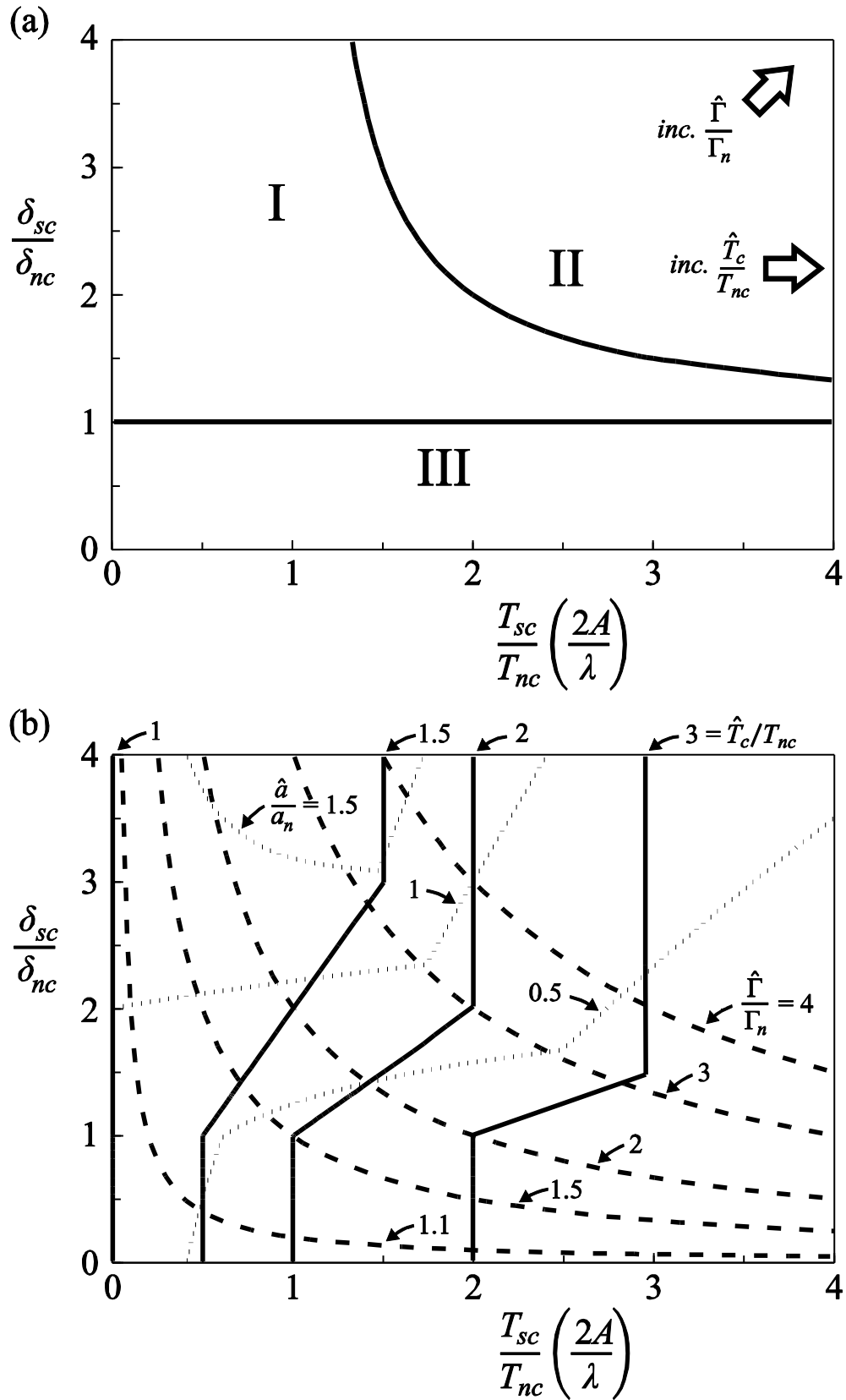


Figure 13. (a) Three regimes of square-wave behaviour are identified. (b) Contours of normalised square-wave traction, energy dissipation and transition flow size illustrate the available property space for square-wave joints.